

A Journal of the Gesellschaft Deutscher Chemiker

Angewandte Chemie

GDCh

International Edition

www.angewandte.org

Accepted Article

Title: In situ Construction of Single-Atom Electronic Bridge on COF to Enhance Photocatalytic H₂ Production

Authors: Jie Li, Jie Zhou, Xiao-Han Wang, Can Guo, Run-Han Li, Huifen Zhuang, Wenhai Feng, Yingjie Hua, and Ya-Qian Lan

This manuscript has been accepted after peer review and appears as an Accepted Article online prior to editing, proofing, and formal publication of the final Version of Record (VoR). The VoR will be published online in Early View as soon as possible and may be different to this Accepted Article as a result of editing. Readers should obtain the VoR from the journal website shown below when it is published to ensure accuracy of information. The authors are responsible for the content of this Accepted Article.

To be cited as: *Angew. Chem. Int. Ed.* **2024**, e202411721

Link to VoR: <https://doi.org/10.1002/anie.202411721>

RESEARCH ARTICLE

WILEY-VCH

In situ Construction of Single-Atom Electronic Bridge on COF to Enhance Photocatalytic H₂ ProductionJie Li,^[b] Jie Zhou,^{*[a]} Xiao-Han Wang,^[b] Can Guo,^[b] Run-Han Li,^{*[b]} Huifen Zhuang,^[b] Wenhai Feng,^[b] Yingjie Hua^[a] and Ya-Qian Lan^{*[b]}^[a] Dr. J. Zhou and Prof. Y. Hua

Key Laboratory of Electrochemical Energy Storage and Energy Conversion of Hainan Province

School of Chemistry and Chemical Engineering

Hainan Normal University

Haikou, 571158, China

E-mail: 920486@hainnu.edu.cn; 20200608@m.scnu.edu.cn

^[b] J. Li, X.-H. Wang, Dr. R.-H. Li, C. Guo, H. Zhuang, W. Feng and Prof. Y.-Q. Lan

Guangdong Provincial Key Laboratory of Carbon Dioxide Resource Utilization

School of Chemistry

South China Normal University

Guangzhou, 510006, P. R. China.

E-mail: lirr949@m.scnu.edu.cn

E-mail: yqlan@m.scnu.edu.cn

Supporting information for this article is given via a link at the end of the document.

Abstract: Photocatalytic hydrogen production is one of the most valuable technologies in the future energy system. Here, we designed a metal-covalent organic frameworks (MCOFs) with both small-sized metal clusters and nitrogen-rich ligands, named COF-Cu₃TG. Based on our design, small-sized metal clusters were selected to increase the density of active sites and shorten the distance of electron transport to active sites. While another building block containing nitrogen-rich organic ligands acted as a node that could in situ anchor metal atoms during photocatalysis and form interlayer single-atom electron bridges (SAEB) to accelerate electron transport. Together, they promoted photocatalytic performance. This represented the further utilization of Ru atoms and was an additional application of the photosensitizer. N₂-Ru-N₂ electron bridge (Ru-SAEB) was created in situ between the layers, resulting in a considerable enhancement in the hydrogen production rate of the photocatalyst to 10.47 mmol g⁻¹ h⁻¹. Through theoretical calculation and EXAFS, the existence position and action mechanism of Ru-SAEB were reasonably inferred, further confirming the rationality of the Ru-SAEB configuration. A sufficiently proximity between the small-sized Cu₃ cluster and the Ru-SAEB was found to expedite electron transfer. This work demonstrated the synergistic impact of small molecular clusters with Ru-SAEB for efficient photocatalytic hydrogen production.

Introduction

Photocatalytic hydrogen production technology is regarded as one of the most promising technologies for the generation of clean energy in the 21st century.^[1] Up to now, an increasing number of catalytic materials have been used for photocatalytic hydrogen production, such as non-metallic oxides,^[2] metal oxides,^[3] metallic sulfides^[4] and their composites, and heterojunction materials.^[5] Although these materials had made great progress in photocatalytic hydrogen production, these photocatalysts still have some problems, such as unclear

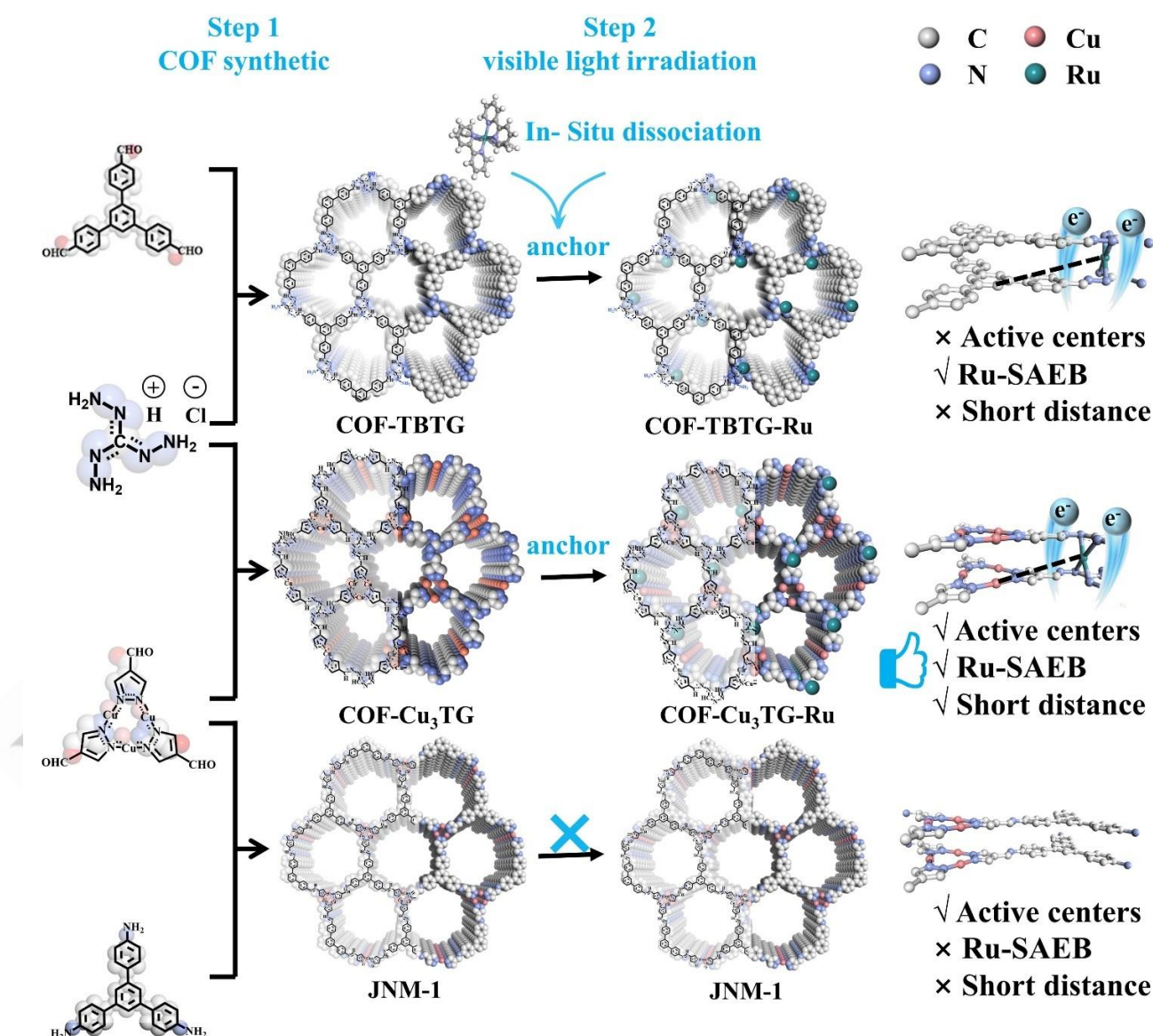
structure, uneven distribution of active sites and lack of clear structural information to identify catalytic sites.^[6] The limited structural recognition will hinder the analysis of active sites in the photocatalytic hydrogen production process, limit the further reasonable design and preparation of the catalyst by scientists.^[7] If reticular chemistry was used as a guiding principle, the synthesis of photocatalysts with precise structures will facilitate further exploration of reaction mechanisms and pathways at the atomic level.^[8]

Covalent organic frameworks (COFs) have played an important role in photocatalysis since they were first reported, due to their advantages of structural design, large surface area, thermal stability and high porosity.^[9] Given that COFs are composed of light elements, their catalytic activity is limited. Various monometallic atoms, including Co^[10], Ni^[11] and Pt^[12], have been embedded into the framework of COFs with the objective of enhancing the hydrogen production rate. However, these approaches are prone to face problems such as the complexity of synthesis steps and the tendency of single atoms to aggregate.^[13] Small-sized metal clusters may be a good choice for solving the above problems due to their unique advantages of well-defined structure, high exposure of active sites and high atomic utilization.^[14] Consequently, metal-covalent organic frameworks (MCOFs) prepared by solvothermal method utilizing small-sized metal clusters as building blocks not only achieve a high degree of dispersion of metal atoms,^[15] but also clarify the number and position of metal atoms in the structure, thereby rendering the structure predictable. Furthermore, they can enhance the stability of individual metal clusters and promote the interaction between clusters, thus improving the photocatalytic efficiency.^[16] Nevertheless, such materials continue to present a challenge in terms of the efficiency of the charge transfer process, which represents a significant obstacle in the design of photocatalysts.

It has been demonstrated that embedding single metal atoms into the layers of MCOFs can form single-atom electron bridge

(SAEB).^[17] It is possible to modify the electron transfer mode from a fully ordered π -array to interlayer ligand-bonded electron transfer, which accelerates the electron transfer rate.^[18] Nevertheless, the post-modified synthesis of SAEB materials will result in a loss of precise regulation of the structure due to the cumbersome synthesis steps and ungente reaction conditions employed, thereby hindering the further development of photocatalysts in photochemical energy conversion.^[19] The in situ controllable synthesis of SAEB offers a distinctive advantage if when the anchor site of the catalyst is designed in advance. Not only can the synthesis steps be simplified, the reaction conditions are mild without damaging the intrinsic structure of the material, but also the anchors can be clarified to facilitate the exploration of the reaction mechanism, etc.^[20] Unfortunately, there are few reports on introducing SAEB in situ into MCOF by designing reserved anchor sites to accelerate the electron transport rate and achieve efficient photocatalytic hydrogen production.

Here, we report the first case of in situ synthesis of SAEB in MCOF for photocatalytic hydrogen production. Based on our elaborate design, we selected small-sized Cu^I cluster and nitrogen-rich organic ligand TG_{Cl} to synthesize a new MCOF catalyst, named $\text{COF-Cu}_3\text{TG}$, for photocatalytic hydrogen production. According to previous reports Cu_3 cluster exhibited strong redox activities, and the SBU triangle structures were not affected even if part of the copper was oxidized, showing good chemical stability. With the addition of $[\text{Ru}(\text{bpy})_3]\text{Cl}_2$ as photosensitizer and triethylamine (TEA) as sacrificial electron donor, visible light-induced hydrogen release was achieved. The hydrogen production increased gradually with the passage of time, and the H_2 production rates of the 1st, 2nd and 3rd hour were ~ 4.19 , ~ 10.47 and ~ 11.88 mmol g^{-1} , respectively. The presence of Ru-SAEB can be used as a fast channel for electron transfer, and the selection of small-sized metal clusters as building blocks not only improves the density of the active sites, but can also shorten the distance between Ru-SAEB and the



Scheme 1. Synthesis and structure diagram of $\text{COF-Cu}_3\text{TG}$, COF-TBTG and JNM-1 , and the process of in situ anchoring of Ru in COFs to form $\text{COF-Cu}_3\text{TG-Ru}$ and COF-TBTG-Ru containing Ru-SAEB.

reaction site, allowing electrons to be rapidly transported to the reaction site. Interaction of the two to jointly increase the rate of production of hydrogen by photocatalysis.^[21] X-ray absorption spectroscopy (XAS) and extended X-ray absorption fine structure (EXAFS) spectroscopy were used to clarify the anchoring of the metal Ru atom to the N-site of the guanidine ligand between layers, forming a SAEB of the N₂-Ru-N₂ species. In addition, the theoretical calculation results also clarified the position of Ru atoms anchored, and confirmed the existence of Ru-SAEB configuration was reasonable. This was consistent with the pre-designed goal of using the synergistic effect of the small molecule building blocks of MCOF and SAEB to improve the efficiency of photocatalytic hydrogen production. The density functional theory (DFT) calculations also confirmed that the Cu cluster was used as the active sites for hydrogen evolution and that Ru-SAEB was used as the channel for electron transfer, which was conducive to achieving efficient visible-light responsive HER. In conclusion, the synergistic effect of the active site of Cu(I) cluster and the single atom electron bridge of N₂-Ru-N₂ greatly improved the efficiency of photocatalytic hydrogen production.

Results and Discussion

To achieve the desired goal, the precursor [Cu₃(PyCA)₃] (1H-PyCA = pyrazolate-4-carboxaldehyde, denoted Cu₃) was synthesized according to previous reports.^[22] As shown in the Scheme 1, COF-Cu₃TG was synthesized by Schiff base condensation reaction of Cu₃ and triamino-guanidine hydrochloride (TG_{Cl}) in a mixture of mesitylene (MES) and N, N-dimethylformamide (DMF) under vacuum solvothermal conditions. It was concluded from the sharp diffraction peak on the powder X-ray diffraction (PXRD) pattern that we had obtained COF-Cu₃TG with high crystallinity (Figure 1a). The 6.4° strong diffraction peak in the PXRD pattern corresponded to (100) crystal facets. Other small peaks correspond to (110) and (001) crystal planes respectively. We used Materials Studio 2019 to simulate the structure. We set up four kinds of structural models, including *P*-6 space group corresponding to AA stacking, *P*-6 space group corresponding to AB stacking, *P*32 space group and *R*-3 space group corresponding to ABC stacking. From the simulated PXRD patterns of various configurations, it was found that the PXRD patterns of COF-Cu₃TG obtained in our experiment are more consistent with the calculated PXRD patterns of AA stacking model, and the curve gap between them and other stacking modes is large. We used Pawley refinements to refine the experimental curve, and determined the unit cell parameter was *a* = *b* = 15.8380 Å, *c* = 3.5051 Å, *α* = *β* = 90°, *γ* = 120°, the difference curve showed the good residual of *R* factor of *R*_p = 2.46% and *R*_{wp} = 3.09%, which once again confirmed the rationality of the simulation. The structural information of the all stacking models is in the Supplementary Information.

In the Fourier-transform infrared (FT-IR) spectra, it was observed that the N-H stretching vibration mode from 3200 cm⁻¹ to 3400 cm⁻¹ of TG_{Cl} and the C=O stretching vibration mode at 1667 cm⁻¹ of Cu₃ disappeared, and the C=N stretching vibration

mode appeared at 1617 cm⁻¹ (Figure 1b).^[23] The above results confirmed the condensation reaction of the two raw materials and the formation of the imine bond, showing the successful synthesis of COF-Cu₃TG. We used field emission scanning electron microscopy (SEM) and high-resolution transmission electron microscopy (HRTEM) to characterize COF-Cu₃TG to determine its morphology. From SEM, it was seen that COF showed a spherical structure formed by thin sheet stacking (Figure 1c, Figure S14). It was greatly different from the needle like Cu₃ and thick sheet like TG_{Cl} structure before synthesis, which once again confirmed the successful synthesis of COF-Cu₃TG (Figures S15-16). HRTEM image was further taken to understand the crystal structure of COF-Cu₃TG, which showed that it was a layered structure with a lattice spacing of 0.34 nm (Figure 1d). The element mapping image confirmed that the elements Cu, C and N was evenly distributed in this COF (Figure 1e). The Brunauer-Emmett-Teller (BET) surface area of COF-Cu₃TG were 388.4 m² g⁻¹, measured by N₂ absorption-desorption at 77 K (Figure S17).

Thermogravimetric analysis (TGA) showed that COF-Cu₃TG, JNM-1 and COF-TBTG all had excellent thermal stability, and there was no obvious weight loss at the decomposition temperature of 200 °C (Figures S18-20). To explore the chemical stability of COF-Cu₃TG, it was immersed in common inorganic solvent and various organic solvent for 72 hours, washed the sample with hexane, and then dried it in vacuum (Figure S21). Obviously, we found that the PXRD patterns of the treated COF-Cu₃TG did not change significantly, and still maintained good crystallinity and stability.

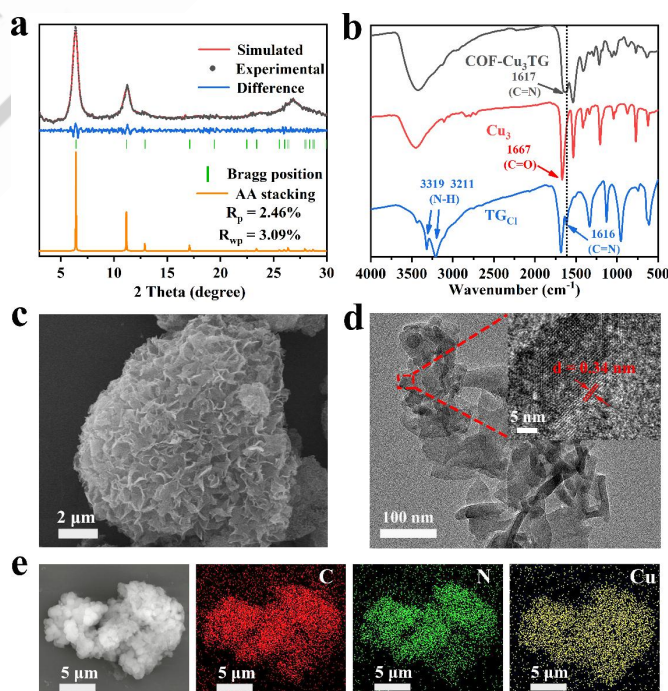


Figure 1. Morphology and structure characterization. **a** PXRD pattern of experimental and simulated COF-Cu₃TG. **b** IR spectra of COF-Cu₃TG, Cu₃ and TG_{Cl}. **c** SEM image and **d** TEM image of COF-Cu₃TG. **e** Element mapping images of COF-Cu₃TG.

For the purpose of analyzing the elemental valence state on the surface of the COF-Cu₃TG catalyst, we carried out the X-ray photoelectron spectroscopy (XPS) to confirm. The characteristic peaks of Cu(I) and Cu(II) were observed in the high-resolution Cu 2p spectrum of COF-Cu₃TG (Figure S22). 932.6 eV and 934.6 eV were attributed to Cu^I 2p_{3/2} and Cu^{II} 2p_{3/2} respectively, while 952.5 eV and 955.6 eV were attributed to Cu^I 2p_{1/2} and Cu^{II} 2p_{1/2}, respectively.^[24] The monomer Cu₃ only had strong and sharp Cu^I signal peaks, but no Cu^{II} signal peaks (Figure S23). Obviously, a small part of Cu^I in the obtained COF-Cu₃TG was oxidized to Cu^{II}. Although some Cu^I was oxidized, it did not affect the SBU triangular structure in any way, and it still maintained a good chemical stability.^[22,24] All the XPS results had been corrected according to the standard C 1s peak at 284.6 eV (Figure S24).

In order to better research, JNM-1^[25] and COF-TBTG^[26] were also synthesized and analyzed as comparison samples, which were synthesized from Cu₃ and TAPB, TG_{Cl} and TFPB, respectively. The UV-vis diffuse reflectance (UV/Vis-DRS) results of these materials were measured. As shown in Figure 2a, all three samples exhibited certain absorption in the visible light region. The Tauc plots were obtained from the UV/Vis-DRS spectra (Figure S25), and then the corresponding optical band gaps (E_g) of COF-Cu₃TG, JNM-1 and COF-TBTG were obtained

as 1.76 eV, 2.02 eV and 2.34 eV, respectively. Combined with Mott-Schottky (M-S) measurements (Figures S26-28), the flatband potential of COF-Cu₃TG, JNM-1 and COF-TBTG were estimated to be -1.25 V, -1.29 V and -1.27 V (vs. Ag/AgCl). The values were further converted to be -1.05 V, -1.09 V and -1.07 V (vs. NHE). In summary, the band structure of the three catalysts was depicted schematically. As can be seen from the Figure 2b, in terms of thermodynamics, all three could complete photocatalytic HER reaction.

The separation and migration rates of photoinduced electron-hole pairs played an important role in photocatalytic hydrogen production. According to transient photocurrent responses (TPR) results (Figure 2c), all three materials had switching photosensitivity and good periodicity. The photocurrent intensity of COF-Cu₃TG was 15 times higher than that of COF-TBTG and 8 times higher than that of JNM-1. From the electrochemical impedance spectroscopy (EIS) measurement results, the Nernst radii of COF-Cu₃TG and JNM-1 were much lower than that of COF-TBTG (Figure S29). To understand the separation and transfer of photocatalyst photocarriers, the photoluminescence spectra (PL) of COF-Cu₃TG, JNM-1 and COF-TBTG excitation were analyzed. In the Figure S30, COF-Cu₃TG showed strong fluorescence intensity. The spectral peak position of both COF-Cu₃TG, JNM-1 and Cu₃ was about 400 nm, which was similar to the previously reported Cu₃-based materials (Figure S31). Meanwhile, in order to explore the average lifetime of photoexcited electrons, time-resolved fluorescence attenuation spectra were made. The results showed that compared with JNM-1 ($t_{avg} = 2.03 \mu s$), COF-TBTG ($t_{avg} = 7.18 \mu s$), the average decay lifetime of COF-Cu₃TG was 6.05 μs (Figures S32-34, Table S5). Although JNM-1 and COF-TBTG had certain photoluminescence properties, COF-Cu₃TG showed stronger photocurrent response, which indicated that COF-Cu₃TG has better charge separation performance. These experimental results proved that COF-Cu₃TG photochemical performance was the best, and it showed better photocatalytic effect with better photosensitivity and higher electron transfer efficiency.

Having determined the structure, basic optical and electrical properties of the COF, we proceeded to investigate their photocatalytic properties for H₂ production. When [Ru(bpy)₃]Cl₂ was added to a mixture of MeCN and water as a photosensitizer and TEA was used as a hole sacrificial electron donor, COF-Cu₃TG showed the excellent photocatalytic capacity to produce H₂ with an average amount of H₂ up to 4193.1 $\mu mol g^{-1} h^{-1}$ (10116.3 $\mu mol g_{Cu}^{-1} h^{-1}$). In contrast, JNM-1 had only 2751.8 $\mu mol g^{-1} h^{-1}$ and COF-TBTG had only 134.5 $\mu mol g^{-1} h^{-1}$ (Figure 2d). Compared with these two materials, the photocatalytic activity of COF-Cu₃TG was 1.5 times and 31.8 times higher, respectively. Meanwhile, the addition of [Ru(bpy)₃]Cl₂ and TEA to the pure water system also produced a certain amount of H₂, but it was relatively low (Figure S35). When triethanolamine (TEOA), triisopropanolamine (TIPA), ethylenediaminetetraacetic acid (EDTA), ascorbic acid (AA), and sodium ascorbate (Asc) were used instead of TEA as sacrificial electron donor, HER efficiency was decreased, indicating that the selection of sacrificial electron donor had a great effect on photocatalytic activity (Figure S36). In order to investigate the effect of different

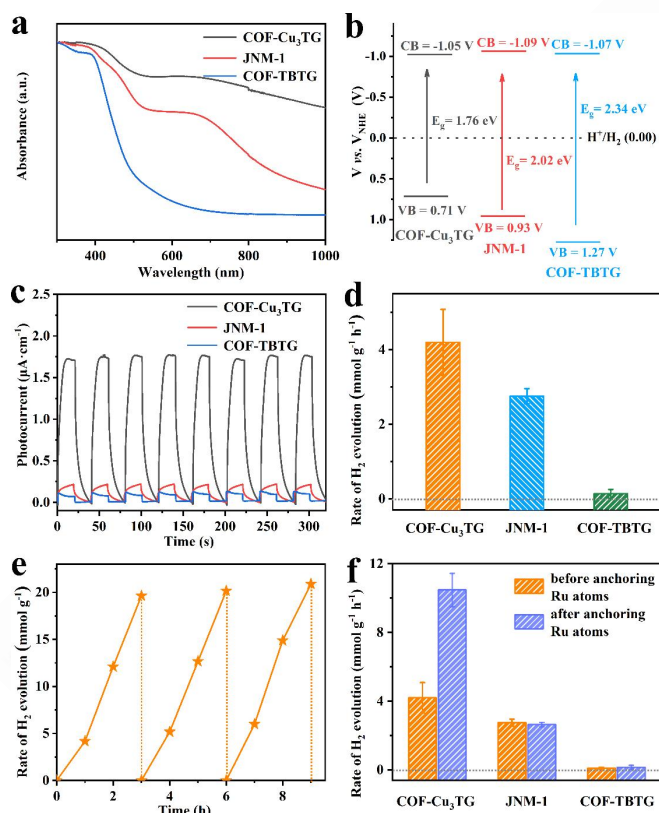


Figure 2. Optoelectronic properties and photohydrolysis properties. **a** UV/Vis-DRS spectra of COFs. **b** Band structure diagram. **c** Transient photocurrent responses. **d** The rate of H₂ formation at a volume ratio of 8:1:1 between MeCN, H₂O and TEA under visible light. **e** Long-term H₂ production. **f** Rate of H₂ evolution before and after anchoring Ru atoms.

MeCN - H₂O ratio on hydrogen production, the HER efficiency of COF-Cu₃TG in the system was investigated. We found that the suitable conditions were an acetonitrile to water ratio of 8: 1, with an average hydrogen production of 4193.1 $\mu\text{mol g}^{-1} \text{h}^{-1}$ (Figure S37).

The photocatalytic hydrogen evolution reaction was further studied after the suitable conditions were selected. It was the same as our assumption that the hydrogen production rate of COF-Cu₃TG will gradually increase with the extension of time (Figure 2e). In order to further confirm the experimental phenomenon, the photocatalytic effects before and after anchoring Ru atoms were compared. The results showed that the photocatalytic hydrogen evolution rate of COF-Cu₃TG-Ru was as high as 10471.8 $\mu\text{mol g}^{-1} \text{h}^{-1}$ (4193.1 $\mu\text{mol g}_{\text{Cu}}^{-1} \text{h}^{-1}$), which was significantly higher than that of COF-Cu₃TG. Importantly, the visible photocatalytic HER activity of COF-Cu₃TG-Ru is also among the top in the recently reported HER materials with the addition of H₂PtCl₄ as a co-catalyst (Table S6). These were completely consistent with our initial assumption that Ru-SABE was formed because a large number of bare N atoms of the organic ligand TG_{Cl} anchored the metal Ru atoms. Although Ru-SABE was also present in COF-TBTG as the control sample, due to the lack of active site, there was no high hydrogen evolution even though the photogenerated electron transfer rate was accelerated, and the hydrogen yield was from 87.59 to 146.85 $\mu\text{mol g}^{-1} \text{h}^{-1}$. However, for JNM-1, due to the lack of a large number of exposed N sites, in situ loading was unsuccessful and there was no change in subsequent reactions (Figure 2f). It was found by EDS that no Ru-SABE was formed under dark conditions (Figure S38). So, the light was also a necessary condition.

When the quantity of [Ru(bpy)₃]Cl₂ was augmented, we observed that the catalytic influence of COF-Cu₃TG-Ru did not improve, reinforcing the notion that [Ru(bpy)₃]Cl₂ solely functions as a light-absorbing agent and the dynamic centre was located on our catalyst (Figure S39). Then the apparent quantum efficiencies (AQE) of COF-Cu₃TG and COF-Cu₃TG-Ru in the photocatalytic process were investigated at different wavelengths. At 420 nm, the aqe value of COF-Cu₃TG-Ru was up to 0.62%, while the aqe value of COF-Cu₃TG was up to only 0.42% (Figure S40).

The corresponding element mapping images further confirmed the rationality of our design. Ru elements were evenly distributed in COF-Cu₃TG-Ru (Figure 3a). Of course, Ru elements were also observed in COF-TBTG-Ru (Figure S41). However, Ru elements were not observed in the element mapping images of JNM-1 after reaction (Figure S42, Table S7), which was consistent with our predesign result that JNM-1 was difficult to form Ru-SABE due to the lack of the N-site of the anchor metal. The content of Ru element in COF-Cu₃TG-Ru and COF-TBTG-Ru was 1.66% and 0.69%, respectively, measured by inductively coupled plasma mass spectrometry (ICP-MS, Table S8).

The chemical states of Ru in COF-Cu₃TG-Ru was further analyzed by XPS. Peaks of 3p and 3d orbits of Ru were observed, which were absent from COF-Cu₃TG (Figure 3b, Figure S43). The new component of COF-Cu₃TG-Ru in 462.0 eV

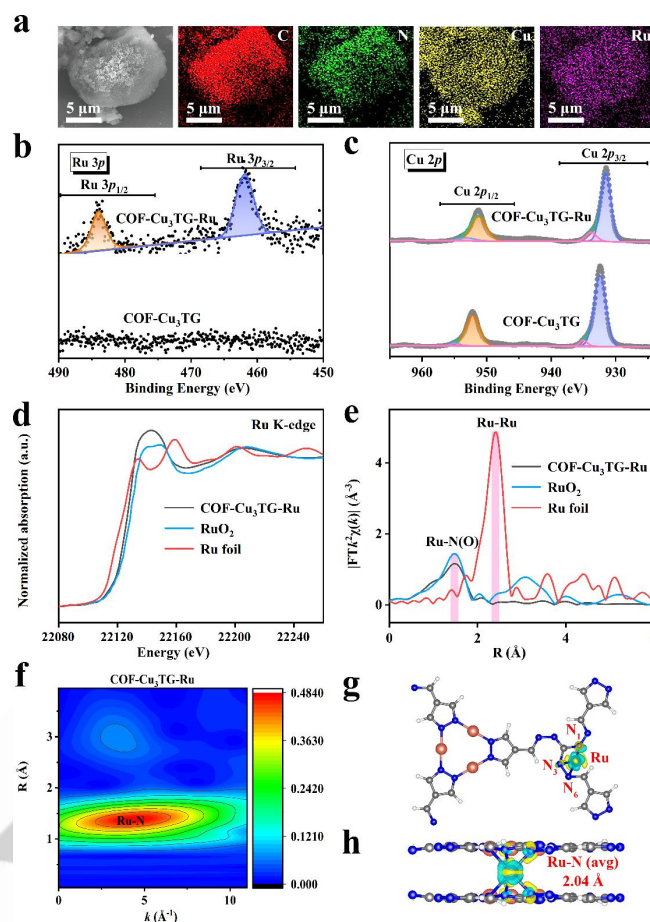


Figure 3. The performance after forming SABE and chemical state of Ru atom. **a** Element mapping images of COF-Cu₃TG-Ru. **b** XPS spectra for Ru 3p. **c** XPS spectra for Cu 2p. **d** Ru K-edge spectra of COF-Cu₃TG-Ru. **e** FT-EXAFS spectra of COF-Cu₃TG-Ru and the reference samples. **f** Wavelet transform (WT) of Ru in COF-Cu₃TG-Ru. **g** Top view and **h** side view of difference of charge density for the most stable adsorption configuration of the minima repeating unit of COF-Cu₃TG-Ru, in which blue and yellow regions indicate electron depletion and accumulation, respectively.

was attributed to Ru 3p_{3/2}, and another 483.9 eV was attributed to Ru 3p_{1/2}, which proves the existence of Ru^{δ+} substances.^[27] After the formation of Ru-SABE, the binding energy of Cu 2p_{3/2} decreased from 932.3 eV to 931.4 eV, indicating that built-in electric field (BIEF) was formed between the Ru and Cu, and Cu obtained electrons (Figure 3c).^[24, 28] Peaks of 3p and 3d orbits of Ru can also be observed at COF-TBTG-Ru (Figures S44-45).

X-ray absorption spectroscopy (XAS) and extended X-ray absorption fine structure (EXAFS) spectra were performed to further clarify the chemical state and coordination environment of Ru in COF-Cu₃TG-Ru. In the X-ray absorption near edge structure (XANES) spectra of K edge, the absorption energy edge of COF-Cu₃TG-Ru lies between Ru foil and RuO₂, indicating that Ru atom in COF-Cu₃TG-Ru carried positive charge and its average oxidation state was between 0 and +4 (Figure 3d). In addition, the Fourier-transform (FT) *k*³-weighted EXAFS spectra of Ru K-edge showed that the main peak of COF-Cu₃TG-Ru at $\approx 1.47 \text{ \AA}$ was attributed to the shell

coordination of the nearest Ru-N bond, and no obvious Ru-Ru peak was found at $\approx 2.42 \text{ \AA}$ (Figure 3e).^[29] It showed that all Ru atoms in the monoatomic form of COF-Cu₃TG were coordinated with N atoms. Compared with Ru foil and RuO₂, Ru-Ru signal was not observed at $\approx 9.5 \text{ \AA}^{-1}$ in the WT diagram of COF-Cu₃TG-Ru (Figure 3f, Figure S46).^[30] The EXAFS fitting curve was carried out and the corresponding parameters were summarized (Figures S47-49). The XPS and EXAFS fitting results were summarized to prove the existence of Ru-N bond, and the least squares EXAFS fitting method was used to simulate the local structural parameters of Ru elements. The simulation results showed that the coordination number of Ru atoms was 6 and the average bond length was about 2.01 \AA (Table. S9). The average valence state of Ru in COF-Cu₃TG-Ru was 3.62 (Figure S50).

In addition, the most probable reasonable structure of Ru-SAEB was determined based on theoretical calculations, and these evidences suggested that Ru atoms in Ru-SAEB coordinate with N in TG_{Cl} in the interlayer (Figure 3g). Combined with the above experimental data, we used DFT to simulate the structure of 5 different chemical states of Ru-SAEB (Figures S51-55).^[31] As shown, COF-Cu₃TG-Ru was most stable when Ru atoms were coordinated with four N atoms at positions N₁ and N₃ in the two TG_{Cl} between layers (Figure S56). Further differential charge density analysis showed that Ru atom only had charge transfer relationship with four N atoms of two types, N₁ and N₃, and the corresponding Ru-N bond length is 2.04 \AA (Figure 3h). There was no obvious charge transfer between N₆ atom at the adjacent position of N₁, and the bond length was also longer (2.21 \AA).^[32]

To investigate the stability of the photocatalyst after SAEB formation, COF-Cu₃TG-Ru and COF-TBTG-Ru were tested by FT-IR and PXRD. We found that the spectra of PXRD and FT-IR were not very different from those before (Figures S57-59), indicating that their structures remained intact. Furthermore, the solid-state ¹³C cross-polarization magic-angle-spinning (CP/MAS) NMR spectra demonstrated that the imine bond in the COF framework was not damaged by the introduction of Ru-SAEB (Figures S60-61).^[33] In addition, durability experiments were performed on COF-Cu₃TG-Ru, and the pristine photocatalytic efficiency for H₂ production was maintained over four consecutive cycles (Figure S62). Once again, the in situ synthesis of SAEB proved absolutely superior in ensuring structural stability and topological prediction. According to the HRTEM image, no Ru or RuO₂ nanoparticles were found (Figure S63), which proved that Ru elements existed in the form of Ru-SAEB in the sample. According to SEM images, COF-Cu₃TG-Ru still maintained a sheet structure (Figure S64), but it was different from the spherical structure of COF-Cu₃TG. This was due to the intense agitation in the process of photocatalysis, the aggregation state had changed, but the sheet structure did not change significantly, which proved its good stability.

Next, the photochemical properties of the catalysts after Ru-SAEB formation were further tested. The UV/vis DRS results showed that the absorption edges of COF-Cu₃TG-Ru and COF-TBTG-Ru were red-shifted (Figure 4a, Figure S65). The results of the photocurrent and EIS test showed that both COF-Cu₃TG-

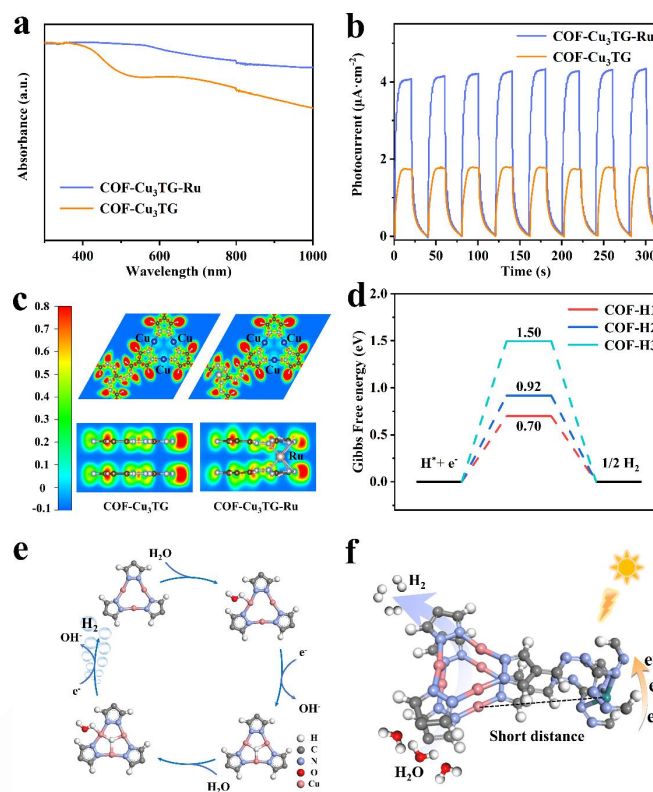


Figure 4. Optoelectronic properties, Mechanism and DFT calculations. **a** The solid-state UV-vis DRS. **b** Transient photocurrent responses. **c** ELF maps of the COF-Cu₃TG and COF-Cu₃TG-Ru. **d** Gibbs Free energy diagram of COF-Cu₃TG-Ru at different hydrogen evolution sites. **e** Simulation of the mechanism of photocatalytic hydrogen evolution. **f** Schematic diagram of the photocatalytic hydrogen production of COF-Cu₃TG-Ru.

Ru had stronger photocurrent corresponding signals (Figure 4b) and smaller Nernst radius than before the formation of electron bridge, indicating that the presence of Ru-SAEB indeed promotes the separation and transmission of photoinduced carriers (Figure S66). PL results showed that the peak positions of the catalyst spectra before and after the formation of Ru-SAEB did not shift significantly (Figures S67-68). Combined with the above results, we found that the presence of N₂-Ru-N₂ did promote the separation and transport of photoinduced carriers. The transient PL decay results showed that COF-Cu₃TG-Ru ($t_{\text{avg}} = 4.81 \text{ \mu s}$) had a lower fluorescence decay rate and a longer fluorescence lifetime compared with COF-TBTG-Ru ($t_{\text{avg}} = 3.60 \text{ \mu s}$) (Figures S69-70). Combined with the above results, we found that the photoelectrochemical performance of COF-Cu₃TG-Ru was more excellent and more conducive to the completion of the photocatalytic hydrogen production process.

To understand the bonding properties of COF-Cu₃TG structure before/after the introduction of Ru atoms, electron localization function (ELF) maps had been carried out in different directions.^[34] As shown in Figure 4c, the projections in the parallel direction of the COF-Cu₃TG showed that the electrons of 3d orbital of Cu atoms were delocalized (iso-surfaces of ELF with the iso-values of 0.1 au), and an obvious interface existed

in the vertical interlayer. When Ru atom was introduced, the chemical bond in the COF-Cu₃TG did not change significantly, but a certain electron delocalization occurred around the Ru atom of the vertical direction.^[34a] In addition, the electron density of adjacent atoms connected with Ru existed obviously polarized, indicating a new covalent interaction between N-Ru atoms. According to the above results, we concluded that the role of Ru-SAEB was to accelerate electron transfer, and the active site for the reduction of H₂O was in Cu sites. In order to judge the Gibbs Free energy of adsorption of H atom, we designed three models with different adsorption H sites (Figures S71-73). By comparing the above models, the energy barrier for adsorption of the H intermediate at the trinuclear Cu center was the lowest, implying that Cu was the most active site for photocatalytic hydrogen production (Figure 4d). Compared with COF-Cu₃TG ($\Delta G = 2.28$ eV), COF-Cu₃TG-Ru had a lower energy barrier ($\Delta G = 0.7$ eV) and a stronger HER activity, suggesting that Ru-SAEB played a positive role (Figures S74). Based on the above calculation and analysis, the preliminary reaction mechanism and pathway were shown in the Figure 4e. Under visible light irradiation, the photosensitizer [Ru(bpy)₃]Cl₂ was excited and the induced electrons were transferred to the catalyst via Ru-SAEB. H₂O was adsorbed at the Cu site, and photogenerated electrons located on COF-Cu₃TG-Ru directly participate in the reduction of H₂O to produce H₂, while the remaining holes were consumed by the sacrificial agent TEA, thus completing a whole cycle.^[35] The presence of Ru-SAEB made the photogenerated electrons migrate to the reaction site at a faster rate, effectively promoting the water decomposition to produce hydrogen. Therefore, the Cu clusters were the active site of photocatalytic water decomposition to produce hydrogen, and the role of the Ru-SAEB was to accelerate electron transport (Figure. 4f).

Conclusion

In summary, in order to maximize the rate of photogenerated electron migration, the in situ introduction of SAEB into MCOF during photocatalysis was achieved for the first time. we designed and synthesized COF-Cu₃TG by choosing small-sized metal clusters and organic ligands containing multiple N sites. As expected, COF-Cu₃TG successfully anchored Ru atoms in situ during the photocatalytic process to form interlayer Ru-SAEB, which accelerated the rate of photogenerated electron migration. Meanwhile, the selection of small-sized metal clusters could improve the utilisation of metal atoms and shorten the distance between Ru-SAEB and the reaction site so that the electrons could be quickly transferred to the reaction site. After working together, the rate of photocatalytic hydrogen production was greatly improved. The hydrogen production rate achieved a substantial increase from the initial 4.19 to 10.47 mmol g⁻¹ h⁻¹ (from 10.12 to 41.93 mmol g_{Cu}⁻¹ h⁻¹). In addition, EXAFS spectroscopy and DFT calculations demonstrated that the Ru atoms were indeed anchored to the N sites in the interlayer, forming a Ru-SAEB, which accelerated the rate of electron transfer and consequently dramatically improved the photocatalytic HER capability. Our study provided a state-of-the-

art paradigm for improving the electron transfer rate and designing efficient photocatalytic systems that could construct catalysts with fast charge transfer rate and excellent activity for efficient solar energy utilization.

Acknowledgements

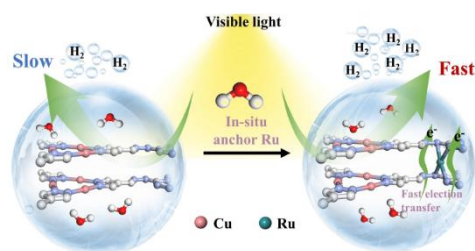
This study was financially supported by the National Key R&D Program of China (2023YFA1507204), the NSFC (Grants 21871141, 21871142, 21901122, 22071109, 22105080, and 92061101), and the Guangdong Basic and Applied Basic Research Foundation (No. 2022A1515110934).

Keywords: covalent organic framework • single-atom electron bridge • photocatalytic hydrogen evolution

- [1] a) M. Herran, S. Juergensen, M. Kessens, D. Hoeing, A. Köppen, A. Castillo, W. J. Parak, H. Lange, S. Reich, F. Schulz, E. Cortés, *Nat. Catal.* **2023**, *6*, 1205–1214; b) Z. Li, T. Deng, S. Ma, Z. Zhang, G. Wu, J. Wang, Q. Li, H. Xia, S.-W. Yang, X. Liu, *J. Am. Chem. Soc.* **2023**, *145*, 8364–8374; c) W. Weng, J. Guo, *Nat. Commun.* **2022**, *13*, 5768.
- [2] a) X. Wang, K. Maeda, A. Thomas, K. Takanabe, G. Xin, J. M. Carlsson, K. Domen, M. Antonietti, *Nat. Mater.* **2009**, *8*, 76–80; b) J. Fu, J. Yu, C. Jiang, B. Cheng, *Adv. Energy Mater.* **2018**, *8*, 1701503; c) G. Dong, L. Zhang, *J. Mater. Chem. A* **2012**, *22*, 1160–1166.
- [3] a) Q. Hu, Y. Liu, W. Li, Y. Wang, W. Liao, H. Zou, J. Li, X. Huang, *Chem. Eng. J.* **2023**, *451*, 138670; b) M. Z. Z. Rahman, F. Raziq, H. Zhang, J. Gascon, *Angew. Chem. Int. Ed.* **2023**, e202305385.
- [4] P. Da, Y. Zheng, Y. Hu, Z. Wu, H. Zhao, Y. Wei, L. Guo, J. Wang, Y. Wei, S. Xi, C.-H. Yan, P. Xi, *Angew. Chem. Int. Ed.* **2023**, *62*, e202301802.
- [5] a) R. Wang, W. Yu, N. Fang, P. Wang, Y. Chu, S. Wu, J. Liang, *Appl. Catal. B* **2024**, *341*, 123284; b) N. Jin, Y. Sun, W. Shi, P. Wang, Y. Nagaoka, T. Cai, R. Wu, L. Dube, H. N. Nyiera, Y. Liu, T. Mani, X. Wang, J. Zhao, O. Chen, *J. Am. Chem. Soc.* **2023**, *145*, 21886–21896; c) D. Wang, Y. Zheng, X. Zhu, D. Ye, Y. Yang, R. Chen, Q. Liao, *ACS Catal.* **2021**, *13*, 10104–10114.
- [6] X. Yan, B. Wang, J. Ren, X. Long, D. Yang, *Angew. Chem. Int. Ed.* **2022**, *61*, e202209583.
- [7] Z. Guo, Y. Yu, C. Li, E. C. dos Santos, T. Wang, H. Li, J. Xu, C. Liu, H. Li, *Angew. Chem. Int. Ed.* **2024**, *63*, e202319913.
- [8] X. Xu, P. Cai, H. Chen, H.-C. Zhou, N. Huang, *J. Am. Chem. Soc.* **2022**, *144*, 18511–18517.
- [9] a) L. Zhang, Q.-H. Zhu, Y.-R. Zhou, S.-L. Wang, J. Fu, J.-Y. Liu, G.-H. Zhang, L. Ma, G. Tao, G.-H. Tao, L. He, *Nat. Commun.* **2023**, *14*, 8181; b) L. Ran, Z. Li, B. Ran, J. Cao, Y. Zhao, T. Shao, Y. Song, M. K. H. Leung, L. Sun, J. Hou, *J. Am. Chem. Soc.* **2011**, *144*, 17097–17109; c) L. Dai, A. Dong, X. Meng, H. Liu, Y. Li, P. Li, B. Wang, *Angew. Chem. Int. Ed.* **2023**, *135*, e202300224.
- [10] R. Chen, Y. Wang, Y. Ma, A. Mal, X.-Y. Gao, L. Gao, L. Qiao, X.-B. Li, L.-Z. Wu, C. Wang, *Nat. Commun.* **2021**, *12*, 1354.
- [11] H. Zhang, Z. Lin, P. Kidkhunthod, J. Guo, *Angew. Chem. Int. Ed.* **2023**, e202217527.
- [12] P. Dong, Y. Wang, A. Zhang, T. Cheng, X. Xi, J. Zhang, *ACS Catal.* **2021**, *11*, 13266–13279.

- [13] a) J. Sun, J. Yang, T. Wang, S. L. Zhang, H. Yuan, W. Zang, Y. Liu, X. Liu, W. Wang, S. Xi, C. H. Kirk, H. Wang, J. Wang, X. Wang, U. Bhat, Z. Liu, S. Wang, Y.-W. Zhang, J. Wang, *Nano lett.* **2024**, *24*, 5206-5213; b) G. Meng, W. Lan, L. Zhang, S. Wang, T. Zhang, S. Zhang, M. Xu, Y. Wang, J. Zhang, F. Yue, Y. Wu, D. Wang, *J. Am. Chem. Soc.* **2023**, *145*, 12884-12893.
- [14] a) Y.-S. Wei, L. Sun, M. Wang, J. Hong, L. Zou, H. Liu, Y. Wang, M. Zhang, Z. Liu, Y. Li, S. Horike, K. Suenaga, Q. Xu, *Angew. Chem. Int. Ed.* **2020**, *59*, 16013-16022; b) S. Chen, L. Huang, Z. Sun, L. Cao, W. Ying, X. Shi, W. Liu, J. Gu, X. Zheng, J. Zhu, Y. Lin, S. Wei, J. Lu, *Small* **2020**, *16*, 2005571.
- [15] J. Dong, X. Han, Y. Liu, H. Li, Y. Cui, *Angew. Chem. Int. Ed.* **2020**, *59*, 13722-13733.
- [16] a) W.-K. Han, Y. Liu, X. Yan, Y. Jiang, J. Zhang, Z.-G. Gu, *Angew. Chem. Int. Ed.* **2022**, *61*, e202208791; b) M. Lu, S.-B. Zhang, M.-Y. Yang, Y.-F. Liu, J.-P. Liao, P. Huang, M. Zhang, S.-L. Li, Z.-M. Su, Y.-Q. Lan, *Angew. Chem. Int. Ed.* **2023**, *62*, e202307632.
- [17] G. Wang, Y. Wu, Z. Li, Z. Lou, Q. Chen, Y. Li, D. Wang, J. Mao, *Angew. Chem. Int. Ed.* **2023**, *62*, e202218460.
- [18] K. Geng, T. He, R. Liu, S. Dalapati, K. T. Tan, Z. Li, S. Tao, Y. Gong, Q. Jiang, D. Jiang, *Chem. Rev.* **2020**, *120*, 8814-8933.
- [19] a) S. M. F. Vilela, J. A. R. Navarro, P. Barbosa, R. F. Mendes, G. Perez-Sanchez, H. Nowell, D. Ananias, F. Figueiredo, J. R. B. Gomes, J. P. C. Tome, F. A. A. Paz, *J. Am. Chem. Soc.* **2021**, *143*, 1365-1376; b) S. Sato, T. Arai, T. Morikawa, K. Uemura, T. M. Suzuki, H. Tanaka, T. Kajino, *J. Am. Chem. Soc.* **2011**, *133*, 15240-15243.
- [20] X. Meng, S. Wang, C. Zhang, C. Dong, R. Li, B. Li, Q. Wang, Y. Ding, *ACS Catal.* **2022**, *12*, 10115-10126.
- [21] Q. Zhou, Y. Guo, Y. Zhu, *Nat. Catal.* **2023**, *6*, 574-584.
- [22] X. Li, J. Wang, F. Xue, Y. Wu, H. Xu, T. Yi, Q. Li, *Angew. Chem. Int. Ed.* **2021**, *60*, 2534-2540.
- [23] X.-C. Lin, Y.-M. Wang, X. Chen, P.-Y. You, K.-M. Mo, G.-H. Ning, D. Li, *Angew. Chem. Int. Ed.* **2023**, *62*, e202306497.
- [24] J. Zhou, J. Li, L. Kan, L. Zhang, Q. Huang, Y. Yan, Y. Chen, J. Liu, S.-L. Li, Y.-Q. Lan, *Nat. Commun.* **2022**, *13*, 4681.
- [25] R.-J. Wei, H.-G. Zhou, Z.-Y. Zhang, G.-H. Ning, D. Li, *CCS Chem.* **2021**, *3*, 2045-2053.
- [26] H.-J. Da, C.-X. Yang, H.-L. Qian, X.-P. Yan, *J. Mater. Chem. A.* **2020**, *8*, 12657-12664.
- [27] a) G. Fang, F. Wei, J. Lin, Y. Zhou, L. Sun, X. Shang, S. Lin, X. Wang, *J. Am. Chem. Soc.* **2023**, *145*, 13169-13180; b) Y. Zhou, F. Wei, H. Qi, Y. Chai, L. Cao, J. Lin, Q. Wan, X. Liu, Y. Xing, S. Lin, A. Wang, X. Wang, T. Zhang, *Nat. Catal.* **2022**, *5*, 1145-1156.
- [28] J. Wang, B. Guo, J. Sun, Y. Zhou, C. Zhao, Z. Wei, J. Guo, *Appl. Catal. B.* **2023**, *324*, 4681.
- [29] a) L. Cao, Q. Luo, J. Chen, L. Wang, Y. Lin, H. Wang, X. Liu, X. Shen, W. Zhang, W. Liu, Z. Qi, Z. Jiang, J. Yang, T. Yao, *Nat. Commun.* **2019**, *10*, 4849; b) C. Rong, X. Shen, Y. Wang, L. Thomsen, T. Zhao, Y. Li, X. Lu, R. Amal, C. Zhao, *Adv. Mater.* **2022**, *34*, 2110103.
- [30] H. Zhang, S. Zuo, M. Qiu, S. Wang, Y. Zhang, J. Zhang, X. W. Lou, *Sci. Adv.* **2020**, *6*, eabb9823.
- [31] G.D. Liberto, G. Pacchioni, *Adv. Mater.* **2023**, *35*, 2307150.
- [32] a) H. Qi, J. Yang, F. Liu, L. Zhang, J. Yang, X. Liu, L. Li, Y. Su, Y. Liu, R. Hao, A. Wang, T. Zhang, *Nat. Commun.* **2021**, *12*, 3295; b) J. Qin, H. Liu, P. Zou, R. Zang, C. Wang, H.L. Xin, *J. Am. Chem. Soc.* **2022**, *144*, 2197-2207.
- [33] M.-Y. Yang, S.-B. Zhang, M. Zhang, Z.-H. Li, Y.-F. Liu, X. Liao, M. Lu, S.-L. Li, Y.-Q. Lan, *J. Am. Chem. Soc.* **2024**, *146*, 3396-3404.
- [34] a) Z. Chen, W. Gong, J. Wang, S. Hou, G. Yang, C. Zhu, X. Fan, Y. Li, R. Gao, Y. Cui, *Nat. Commun.* **2023**, *14*, 5363; b) F. Ye, S. Zhang, Q. Cheng, Y. Long, D. Liu, R. Paul, Y. Fang, Y. Su, L. Qu, L. Dai, C. Hu, *Nat. Commun.* **2023**, *14*, 2040.
- [35] a) Z. Geng, T. Bo, W. Zhou, X. Tan, J. Ye, T. Yu, *Small* **2023**, *19*, 2206673; b) Z. Zeng, Y. Su, X. Quan, W. Choi, G. Zhang, N. Liu, B. Kim, S. Chen, H. Yu, S. Zhang, *Nano Energy* **2020**, *69*, 104409.

Entry for the Table of Contents



During the photocatalytic process, Ru atoms are anchored in situ by COF-Cu₃TG, forming a single-atom electronic bridge between layers. This, combined with the selection of small-sized metal cluster, facilitate the transfer of photogenerated electrons, significantly enhancing the photocatalytic HER capability.

Keywords: Covalent Organic Framework; Cluster; Single-Atom Electron Bridge; Photocatalytic Hydrogen Production; Molecular Junction.